Theor Chem Acc (2011) 129:105–118
DOI 10.1007/s00214-011-0903-2

REGULAR ARTICLE

A computational study of the radical–radical reaction of $O(^3P)$ + C_2H_5 with comparisons to gas-phase kinetics and crossed-beam experiments

Se-Hee Jung · Yong-Pal Park · Kyoo-Weon Kang · Min-Jin Park · Jong-Ho Choi

Received: 8 January 2011 / Accepted: 4 February 2011 / Published online: 23 February 2011

Abstract We present density functional theory (DFT) and complete basis set (CBS) calculations of the prototypical radical–radical reaction of ground–state atomic oxygen [$O(^3P)$] with ethyl (C_2H_5) radicals. The respective reaction mechanisms and dynamics were investigated on the doublet potential energy surfaces using the DFT method and CBS model. In the title reaction, the barrierless addition of $O(^3P)$ to C_2H_5 led to the formation of energy-rich intermediates that underwent subsequent isomerization and decomposition to yield various products. The products predicted to be found were: $H_2CO + CH_3$, $CH_3CHO + H$, $c\text{–}CH_2OCH_2 + H$, $^{1,3}CH_3COH + H$, $^{1,3}HCOH + CH_3$, $CH_2CHOH + H$, $C_2H_3 + H_2O$, and $CH_2CH_2 + OH$. In particular, unlike previous kinetic results, proposed to proceed only through the direct H-atom abstraction process, two distinctive pathways to the formation of $CH_2CH_2 + OH$ were predicted to be in competition: direct, barrierless H-atom abstraction mechanism versus addition process. The competition was consistent with the recent crossed-beam investigations, and their microscopic dynamic characteristics are discussed at the molecular level.

Keywords Ab initio calculation · Radical–radical reactions · Reaction dynamics · Crossed-beam

S.-H. Jung · Y.-P. Park · K.-W. Kang · M.-J. Park · J.-H. Choi (✉)
Department of Chemistry, Research Institute for Natural Sciences, Korea University, 1, Anam-dong, Seoul 136-701, Korea
e-mail: jhc@korea.ac.kr

1 Introduction

Gas-phase radical–radical reaction dynamics play a significant role in understanding the mechanisms of elementary reactive processes including combustion, hydrocarbon synthesis, interstellar space, and atmospheric chemistry. Despite their mechanistic importance, there have been few theoretical and experimental studies of such radical–radical reactive scattering processes at the molecular level, particularly in the field of reaction dynamics. Most gas-phase experimental investigations conducted thus far are related to bulk kinetics under thermally relaxed conditions. This limited progress is primarily due to the difficulties involved in satisfying the critical prerequisites, which include generation of sufficient amounts of clean hydrocarbon radicals and the implementation of reliable and facile characterization schemes [1].

Several bimolecular scattering experimental studies of oxidation reactions have been reported so far. Donalson and coworkers studied the exoergic reactions of $O(^3P)$ with vinyl (C_2H_3) radicals using arrested relaxation FT-IR spectroscopy and observed the reaction products with strongly nonstatistical vibrational distributions [2]. Bersohn et al. investigated the reactions of $O(^3P)$ with methyl (CH_3) radicals under low-pressure flow conditions using the spectroscopic method and favored an indirect addition mechanism to explain the rovibrationally excited states of the products [3]. Leone and coworkers studied the reactions of $O(^3P)$ with alkyl radicals using time-resolved FT-IR spectroscopy and observed the OH products [4, 5]. Direct abstraction and indirect addition mechanisms were proposed to account for the nonstatistical vibrational distributions of the products. Several groups have performed gas-phase kinetic studies to obtain the rate constants and branching ratios using mass spectrometry and laser

spectroscopy [6–8]. In recent years, Choi and coworkers carried out a series of reaction dynamics studies on the oxidation reactions of $O(^3P)$ with saturated ethyl (C_2H_5) and *t*-butyl (*t*-C_4H_9) hydrocarbon radicals and unsaturated π-conjugated hydrocarbon radicals such as allyl (C_3H_5) and propargyl (C_3H_3), using high-resolution laser spectroscopy in a crossed-beam configuration [9–19]. A supersonic flash pyrolysis source was adopted to produce clean, jet-cooled radical beams without experiencing recombination and/or secondary dissociation [20]. Analyses of the nascent state distributions of the various reaction products demonstrated the existence of unusual reaction pathways and dynamic features. These distinctive aspects were found to be in sharp contrast with those of the oxidation reactions of closed-shell hydrocarbon molecules [21–24].

In contrast, only a few theoretical studies of radical–radical oxidation reaction dynamics have been reported. Knyazev and Leone et al. carried out quantum chemical and classical trajectory calculations in an attempt to understand the oxidation reaction of CH_3 radicals, respectively [25, 26]. Yagi and coworkers studied the role of nonadiabatic transitions in the fast reaction: $O(^3P) + CH_3 \rightarrow CH_3O$ [27]. Harding et al. performed quantum chemical and classical trajectory calculations in an attempt to obtain high-pressure recombination rate constants [28]. Gupta et al. and Yang et al. carried out independent ab initio calculations on a few reaction channels of $O(^3P) + C_2H_5$ [29, 30]. With the aid of quantum statistical calculations, Choi and coworkers performed ab initio calculations on the oxidation reactions of allyl, propargyl and *t*-butyl radicals in order to elucidate the reaction mechanisms, kinetics, and dynamic characteristics [31–33].

In this work, the extensive ab initio investigations of the prototypical oxidation reaction of $O(^3P)$ with ethyl (C_2H_5) radicals are described. This study was motivated by this laboratory's efforts to understand the reaction dynamics of gas-phase organic hydrocarbon radicals and to identify the general principles that determine their reactivity and mechanisms [10–19]. Apart from their fundamental importance in elementary reactive scattering processes, the oxidation reaction of the ethyl radical is an important pathway under lean fuel conditions. Therefore, theoretical studies can provide significant mechanistic insights into the oxidation reaction dynamics of saturated hydrocarbon radicals at the molecular level as a model system.

According to the ab initio calculations described herein, several pathways were predicted to be accessible through the following channels:

$$O(^3P) + C_2H_5 \rightarrow H_2CO\,(\text{formaldehyde}) + CH_3 \quad \Delta H = -81.1\ \text{kcal mol}^{-1}, \tag{R1}$$

$$\rightarrow CH_3CHO\,(\text{acetaldehyde}) + H \quad \Delta H = -77.3\ \text{kcal mol}^{-1}, \tag{R2}$$

$$\rightarrow \text{c-}CH_2OCH_2\,(\text{oxirane}) + H \quad \Delta H = -50.7\ \text{kcal mol}^{-1}, \tag{R3}$$

$$\rightarrow {}^1CHOH + CH_3 \quad \Delta H = -23.8\ \text{kcal mol}^{-1}, \tag{R4}$$

$$\rightarrow {}^3CHOH + CH_3 \quad \Delta H = -2.1\ \text{kcal mol}^{-1}, \tag{R5}$$

$$\rightarrow {}^1CH_3COH + H \quad \Delta H = -25.8\ \text{kcal mol}^{-1}, \tag{R6}$$

$$\rightarrow {}^3CH_3COH + H \quad \Delta H = -4.8\ \text{kcal mol}^{-1}, \tag{R7}$$

$$\rightarrow CH_2CHOH\,(\text{ethenol}) + H \quad \Delta H = -65.8\ \text{kcal mol}^{-1}, \tag{R8}$$

$$\rightarrow C_2H_3 + H_2O \quad \Delta H = -75.8\ \text{kcal mol}^{-1}, \tag{R9}$$

$$\rightarrow CH_2CH_2\,(\text{ethene}) + OH \quad \Delta H = -67.3\ \text{kcal mol}^{-1}, \tag{R10}$$

where the reaction enthalpies were determined using our ab initio heats of formation at 298.15 K. In the previous mass spectroscopy experiments conducted by Gutman and coworkers, the temperature-independent rate constant of $2.2 \pm 0.4 \times 10^{-10}$ cm^3 molecule^{-1} s^{-1} for the title reaction was obtained over a temperature range of 295–600 K, and the branching fraction was estimated to be 0.32, 0.40, and 0.23 for the three respective channels (R1), (R2), and (R10) [6, 34]. The high reaction rate suggests that the title reaction proceeds through fast, irreversible association–fragmentation mechanisms. In particular, the reaction channel (R10) was proposed to proceed only through a direct H-atom abstraction pathway.

In the present paper, the computational methods employed are initially described. Afterward, the respective reaction mechanisms on the doublet potential energy surface are presented. In addition, on the basis of the population analysis and comparison with the statistical theory, the results are compared with the experimental results reported in gas-phase kinetics and recent crossed-beam investigations in an attempt to understand the kinetic and dynamic characteristics of the title radical–radical reaction. Finally, the conclusions are presented.

2 Computational methods

Ab initio and statistical calculations were carried out to ascertain the reaction mechanisms, the major reaction pathways, and the kinetic and dynamic characteristics on the lowest doublet potential energy surfaces (PESs) for the title reaction of $O(^3P) + C_2H_5$. The density functional method and complete basis set (CBS) model were employed [35–41]. Various geometries of local minima and transition states along the reaction coordinates were optimized at the hybrid density functional B3LYP levels using the

6–311G(d) and 6–311 + G(3df,2p) basis sets as the initial guesses. In addition, the vibration frequencies were also computed to characterize the stationary points and zero-point energy (ZPE) corrections with a scaling factor of 0.98. To locate the transition structures, the synchronous transit-guided quasi-Newton method was utilized, by which a starting structure for transition state optimization was automatically generated based upon the connection of the transition structure to the reactants and products. All transition states were verified by determination of both the single imaginary frequency and the connections between the designated reactants and products through intrinsic reaction coordinate calculations. Afterward, the complete basis set model of CBS-QB3 was employed to perform more reliable calculations. Unless otherwise specified, the single-point energies computed at the CBS-QB3 levels are presented in the discussion below. All calculations were performed using the Gaussian 03 system of programs on an IBM-PC and Compaq-Workstation (XP-1000) [42].

3 Results and discussion

The optimized structures of the reactants, products, intermediates, and transition states involved in pathways (R1)–(R10) of the title reaction $O(^3P) + C_2H_5$ are shown in Figs. 1 and 2. The ZPE-corrected energies, relative to the reactants at various levels of theory and their scaled harmonic vibrational frequencies, are also listed in Tables 1 and 2, respectively. Here, it should be noted that in comparison with the heats of formation and reaction enthalpies calculated on a few channels reported by Gupta et al. and Yang et al. [29, 30] as clearly manifested in Table 1, the estimated values herein were in strong agreement with the previously reported experimental values within an accuracy of 1.5 kcal mol^{-1}.

Figure 3 shows a diagram of the different pathways on the lowest doublet PES. The diagram displays two characteristic reaction mechanisms: addition versus abstraction. Four addition intermediates responsible for reactions (R1)–(R10) are involved in the addition processes, and there exists only one competing abstraction pathway related to the direct H-atom transfer reaction, leading to formation of $CH_2CH_2 + OH$ in reaction (R10). As atomic oxygen attacks C_2H_5 along the entrance reaction coordinate, the strong, long-range attractive interactions between the two open-shell radical reactants result in the formation of an energized C_2H_5O intermediate denoted as eINT1. This overall association process was estimated to be highly exothermic by -92.7 kcal mol^{-1} with respect to the

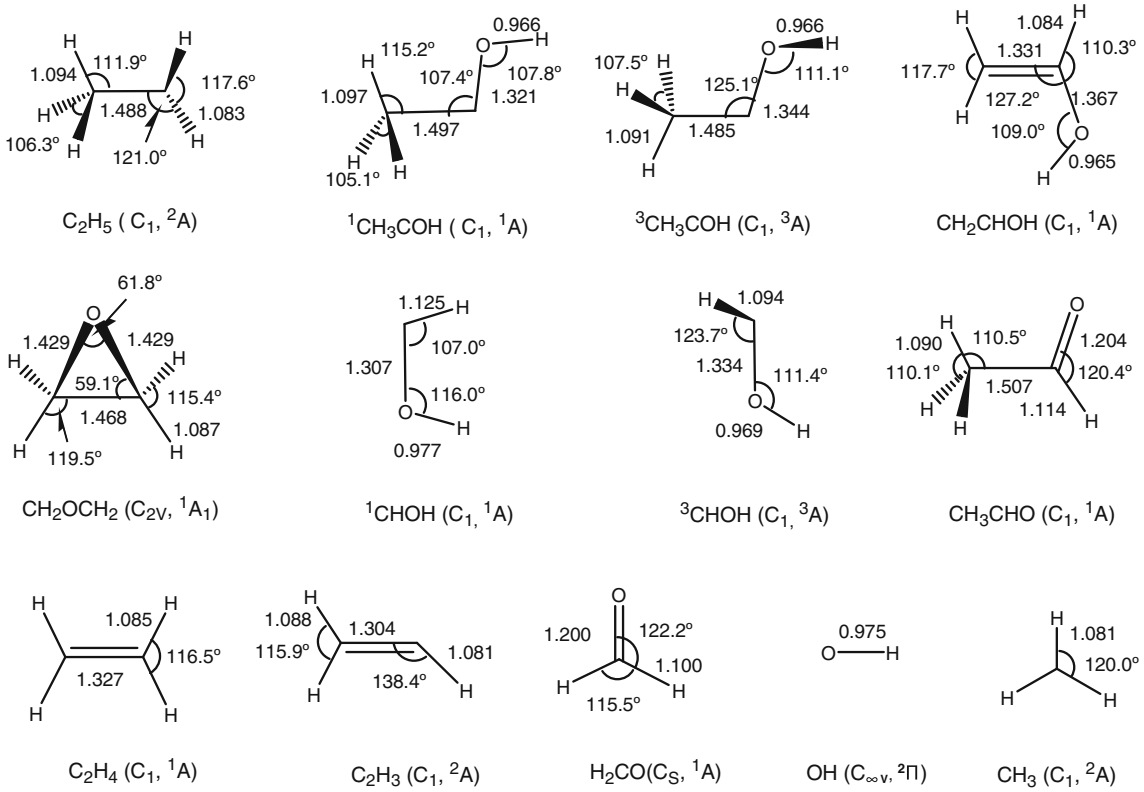

Fig. 1 Optimized geometries of the reactant and products for $O(^3P) + C_2H_5$ at the CBS-QB3 level of theory. Symmetry and electronic terms for each optimized geometry are shown in *parentheses*

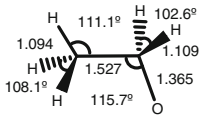

eINT1 (-92.7 kcal mol^{-1}, C_1 , ^2A)

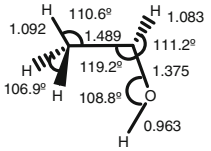

eINT2 (-102.3 kcal mol^{-1}, C_1, ^2A)

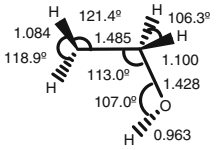

eINT3 (-95.4 kcal mol^{-1}, C_1, ^2A)

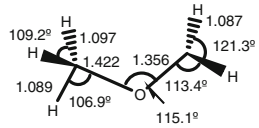

eINT4 (-89.7 kcal mol^{-1}, C_1, ^2A)

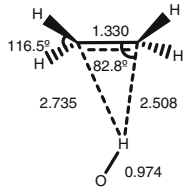

etC (-69.1 kcal mol^{-1}, C_1, ^2A)

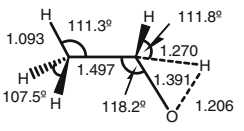

αTS (-65.5 kcal mol^{-1}, C_1, ^2A)

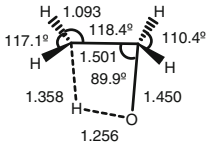

βTS (-64.7 kcal mol^{-1}, C_1, ^2A)

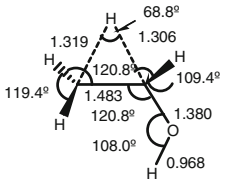

γTS (-56.7 kcal mol^{-1}, C_1, ^2A)

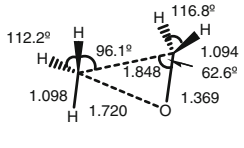

δTS (-42.1 kcal mol^{-1}, C_1, ^2A)

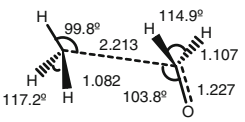

fTS1 (-76.5 kcal mol^{-1}, C_1, ^2A)

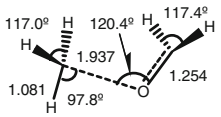

fTS2 (-63.8 kcal mol^{-1}, C_1, ^2A)

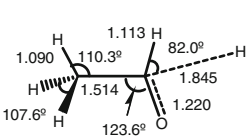

aTS1 (-72.6 kcal mol^{-1}, C_1, ^2A)

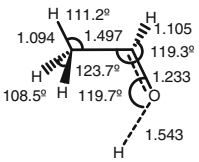

aTS2 (-68.1 kcal mol^{-1}, C_1, ^2A)

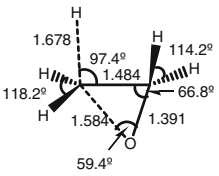

oTS1 (-40.5 kcal mol^{-1}, C_1, ^2A)

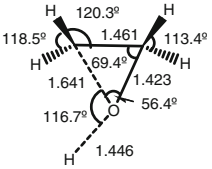

oTS2 (-35.8 kcal mol^{-1}, C_1, ^2A)

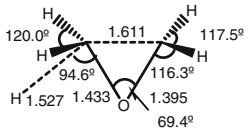

oTS3 (-31.9 kcal mol^{-1}, C_1, ^2A)

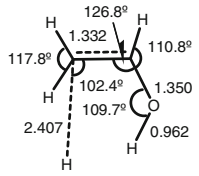

eTS1 (-63.6 kcal mol^{-1}, C_1, ^2A)

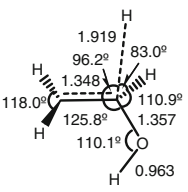

eTS2 (-63.4 kcal mol^{-1}, C_1, ^2A)

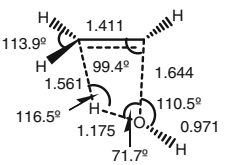

wTS1 (-26.2 kcal mol^{-1}, C_1, ^2A)

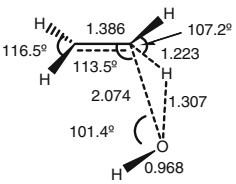

wTS2 (-23.1 kcal mol^{-1}, C_1, ^2A)

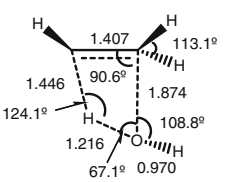

wTS3 (-21.0 kcal mol^{-1}, C_1, ^2A)

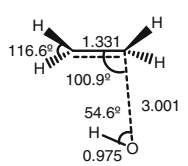

etTS (-69.1 kcal mol^{-1}, C_1, ^2A)

◀ **Fig. 2** Optimized geometries of the intermediates and transition states at the CBS-QB3 level of theory. The values in *parentheses* denote the ZPE-corrected total energies relative to $O(^3P) + C_2H_5$ at 298.15 K, together with symmetry and electronic terms

reactants. Due to the plentiful internal energy, eINT1 can undergo further, different isomerization steps leading to the formation of another three isomers, eINT2, eINT3, and eINT4. As shown in Fig. 4, eINT1 might undergo H-atom migration from either C(1) or C(2) to the oxygen atom to form eINT2 (CH_3CHOH) and eINT3 (CH_2CH_2OH) by overcoming the respective three- and four-membered transition states, αTS and βTS. The respective barrier heights were calculated to be 27.2 and 28.0 kcal mol^{-1} and belong in the typical range of 20–40 kcal mol^{-1} for H-atom migration processes. The isomers, eINT2 and

Table 1 ZPE-corrected total energies (in kcal mol^{-1}) of the various species relative to $O(^3P) + C_2H_5$ at various levels of theory at 298.15 K. The estimated heats of formation and reaction enthalpies were in strong agreement with the previously reported experimental values within the accuracy of 1.5 kcal mol^{-1}

Species	CBS-QB3	CBS-QB3[a]	B3LYP/6–311**[a]	QCISD(T)/6–311 + G(d,p)[b]	Experiment
$O(^3P) + C_2H_5$	0.0	0.0	0.0	0.0	0.0
CH_3CH_2O (eINT1)	−92.7	−88.6	−89.8	−85.6	
CH_3CHOH (eINT2)	−102.3	−97.2	−96.3	−94.8	
CH_2CH_2OH (eINT3)	−95.4	−90.4	−90.0	−87.8	−95.1
CH_3OCH_2 (eINT4)	−89.7			−81.3	−87.7
etC	−69.1				
H_2CO (formaldehyde) + CH_3	−81.1	−83.3	−77.8	−71.7	−78.6
CH_3CHO (acetaldehyde) + H	−77.3	−79.6	−71.4	−66.5	−75.4
c–CH_2OCH_2 (oxirane) + H	−50.7	−51.4	−40.9		−48.3
$^1CHOH + CH_3$	−23.8				
$^3CHOH + CH_3$	−2.1				
$^1CH_3COH$ + H	−25.8				
$^3CH_3COH$ + H	−4.8				
CH_2CHOH (ethenol) + H	−65.8			−54.7	
$C_2H_3 + H_2O$	−75.8				−74.1
CH_2CH_2 (ethene) + OH	−67.3	−72.4	−62.3	−60.1	−66.3
αTS	−65.5[c]	−63.0	−59.7		
βTS	−64.7[c]	−61.5	−58.4	−52.9	
γTS	−56.7[c]	−54.5	−50.5	−44.2	
δTS	−42.1[c]			−29.2	
fTS1	−76.5[c]	−74.3	−72.0	−64.9	
fTS2	−63.8[c]			−51.7	
aTS1	−72.6[c]	−72.8	−66.4	−58.7	
aTS2	−68.1[d]			−53.7	
oTS1	−40.5[c]				
oTS2	−35.8[c]	−35.38	−28.9		
oTS3	−31.9[c]				
eTS1	−63.6[e]				
eTS2	−63.4[c]			−48.5	
wTS1	−26.2[e]				
wTS2	−23.1[c]				
wTS3	−21.0[e]				
etTS	−69.1[e]				

[a] Ref. [29]

[b] Ref. [30]

[c] Calculated using the B3LYP/6–311G(d) basis set

[d] Calculated using the B3LYP/6–311 + G(3fd,2p) basis set

[e] Calculated using the B3LYP/6–311 + G(3fd,2p) basis set

Table 2 Summary of scaled harmonic frequencies and ZPEs of species involved in the reaction of $O(^3P) + C_2H_5$ at 298.15 K using the 6–311G(d) basis set at the CBS-QB3 level of theory

Species	Frequency (cm^{-1})[a]	ZPE (kcal mol^{-1})
C_2H_5[b]	106, 476, 813, 980, 1,062, 1,191, 1,401, 1,465, 1,483, 1,483, 2,943, 3,035, 3,078, 3,139, 3,239	36.6
H_2CO[b]	1,202, 1,270, 1,539, 1,827, 2,869, 2,919	16.5
CH_3CHO[b]	161, 508, 777, 882, 1,125, 1,135, 1,374, 1,426, 1,460, 1,471, 1,824, 2,857, 3,022, 3,077, 3,137	34.3
CH_2CH_2[b]	834, 973, 973, 1,066, 1,238, 1,380, 1,472, 1,692, 3,122, 3,137, 3,193, 3,222	31.6
CH_2CHOH[b]	479, 493, 715, 824, 961, 999, 1,127, 1,328, 1,360, 1,449, 1,703, 3,139, 3,184, 3,238, 3,802	35.1
c–CH_2OCH[b]	817, 846, 890, 1,039, 1,139, 1,142, 1,167, 1,171, 1,300, 1,504, 1,541, 3,078, 3,086, 3,159, 3,174	35.5
$^1CH_3COH$[b]	106, 511, 737, 912, 979, 1,051, 1,294, 1,339, 1,374, 1,445, 1,465, 2,986, 3,067, 3,074, 3,763	34.1
$^3CH_3COH$[b]	172, 308, 403, 894, 1,004, 1,075, 1,158, 1,345, 1,384, 1,458, 1,467, 2,940, 2,984, 3,101, 3,658	33.0
^1CHOH[b]	1,022, 1,210, 1,335, 1,477, 2,722, 3,521	16.0
^3CHOH[b]	461, 1,077, 1,156, 1,300, 3,045, 3,671	15.2
C_2H_3[b]	713, 820, 922, 1,047, 1,391, 1,651, 3,037, 3,133, 3,231	22.6
CH_3[b]	506, 1,403, 1,403, 3,104, 3,283, 3,283	18.4
OH[b]	3,705	5.2
H_2O[b]	1,639, 3,808, 3,906	13.2
etC[b]	5, 71, 119, 283, 323, 835, 987, 994, 1,069, 1,239, 1,379, 1,474, 1,683, 3,126, 3,139, 3,198, 3,226, 3,642	37.9
αTS[c]	2,008i, 184, 425, 601, 871, 900, 1,060, 1,111, 1,172, 1,357, 1,403, 1,470, 1,483, 2,400, 2,994, 3,048, 3,069, 3,112	37.7
βTS[c]	1,985i, 350, 720, 821, 923, 962, 1,072, 1,073, 1,151, 1,208, 1,300, 1,429, 1,530, 1,929, 3,037, 3,082, 3,110, 3,219	38.1
γTS[c]	1,908i, 247, 434, 435, 671, 768, 928, 1,079, 1,199, 1,286, 1,322, 1,395, 1,431, 2,148, 3,130, 3,134, 3,247, 3,705	37.6
δTS[c]	2,008i, 184, 425, 601, 871, 900, 1,060, 1,111, 1,172, 1,357, 1,403, 1,470, 1,483, 2,400, 2,994, 3,048, 3,069, 3,112	37.7
etTS[e]	136i, 37, 75, 219, 448, 836, 973, 984, 1,072, 1,242, 1,377, 1,474, 1,679, 3,125, 3,140, 3,201, 3,233, 3,706	38.0
fTS1[c]	342i, 137, 267, 499, 547, 600, 896, 1,105, 1,249, 1,410, 1,428, 1,489, 1,636, 2,880, 2,925, 3,092, 3,256, 3,268	37.8
fTS2[c]	559i, 83, 140, 295, 647, 686, 930, 992, 1,217, 1,348, 1,425, 1,430, 1,557, 2,955, 3,033, 3,094, 3,252, 3,265	37.3
aTS1[c]	810i, 178, 386, 453, 501, 810, 896, 1,098, 1,125, 1,375, 1,402, 1,464, 1,474, 1,695, 2,851, 3,022, 3,090, 3,135	35.3
aTS2[d]	1,209i, 84, 182, 482, 594, 754, 910, 1,088, 1,122, 1,374, 1,402, 1,455, 1,472, 1,652, 2,947, 3,001, 3,071, 3,130	35.0
oTS1[c]	1,097i, 394, 527, 657, 808, 928, 1,084, 1,147, 1,154, 1,167, 1,195, 1,249, 1,464, 1,529, 3,040, 3,115, 3,140, 3,250	36.6
oTS2[c]	1,313i, 92, 502, 765, 774, 886, 890, 987, 1,132, 1,179, 1,190, 1,282, 1,474, 1,538, 3,058, 3,126, 3,157, 3,270	35.8
oTS3[c]	1,304i, 469, 568, 712, 792, 950, 1,028, 1,068, 1,153, 1,164, 1,216, 1,220, 1,449, 1,504, 3,048, 3,062, 3,166, 3,180	36.4
eTS1[e]	193i, 132, 180, 472, 487, 731, 837, 963, 997, 1,128, 1,323, 1,351, 1,441, 1,685, 3,152, 3,193, 3,255, 3,836	36.0
eTS2[e]	742i, 393, 451, 457, 498, 675, 800, 958, 1,023, 1,123, 1,311, 1,353, 1,447, 1,608, 3,145, 3,192, 3,248, 3,809	36.1
wTS1[e]	1,760i, 327, 434, 546, 658, 746, 812, 891, 1,063, 1,177, 1,278, 1,330, 1,468, 1,692, 3,068, 3,145, 3,168, 3,714	36.5
wTS2[c]	2,390i, 49, 245, 452, 620, 691, 701, 805, 961, 1,005, 1,214, 1,422, 1,459, 2,101, 3,083, 3,125, 3,170, 3,771	35.6
wTS3[e]	1,929i, 222, 412, 546, 621, 722, 787, 948, 997, 1,107, 1,236, 1,345, 1,465, 1,682, 3,039, 3,129, 3,158, 3,756	35.6

[a] i represents imaginary frequency

[b] Calculated using the CBS-QB3 basis set

[c] Calculated using the B3LYP/6–311G(d) basis set

[d] Calculated using the 6–311 + G(d,f) basis set

[e] Calculated using the 6–311 + G(3fd,2p) basis set

eINT3, are slightly lower in energy than eINT1 by 9.6 and 2.7 kcal mol^{-1}, respectively. Here, eINT2 and eINT3 were calculated to be mutually convertible by overcoming the barrier height of 45.6 kcal mol^{-1} for the formation of the three-membered transition state γTS. The fourth intermediate, eINT4 (CH_2OCH_3), is an ether species that is slightly higher in energy than eINT1 by 3.0 kcal mol^{-1}. The eINT4 might be formed by the insertion of an O-atom between the C(1)–C(2) bond of eINT1, through an O-atom bridged δTS with a barrier height of 50.6 kcal mol^{-1}. Since the four addition intermediates possess plentiful internal energy due to their deep potential wells relative to the reactants, they would clearly not be expected to redissociate into the radical reactants, but rather undergo subsequent isomerization or decomposition steps that lead to a variety of products in reactions (R1)–(R10).

Herein, the respective addition reaction mechanisms for pathways (R1)–(R10) are first described through the four

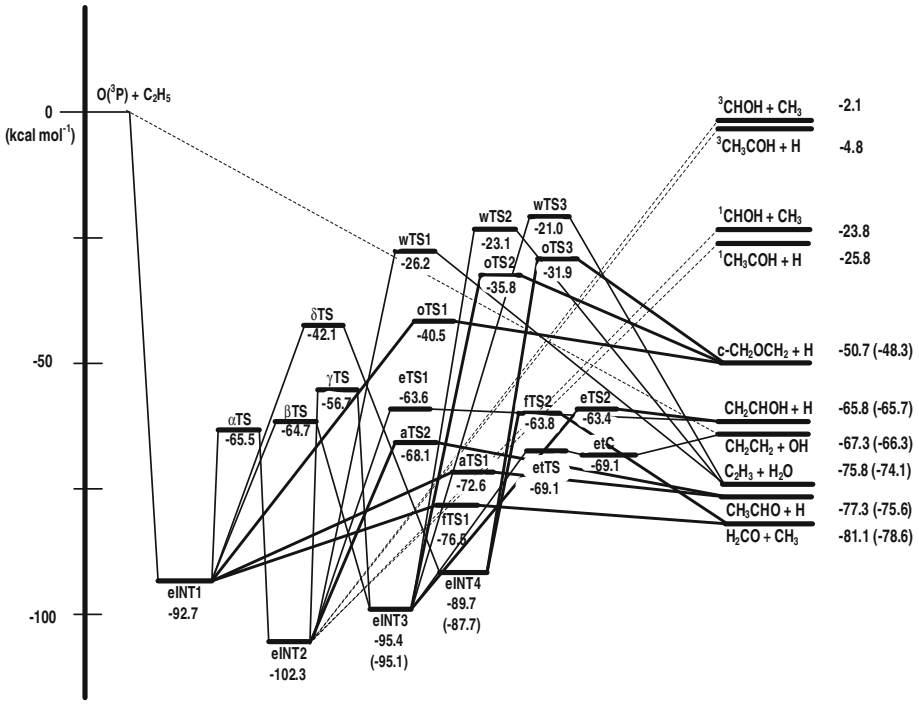

Fig. 3 Schematic energy presentation for the potential energy surface of reaction channels (R1)–(R10) at 298.15 K at the CBS-QB3 level of theory. The values in *parentheses* denote the experimental values in kcal mol^{-1}

energy-rich intermediates eINT1–eINT4. After describing the H-atom abstraction for the production of OH in (R10), the kinetic and dynamic characteristics are compared to the gas-phase kinetics and recent crossed-beam experimental results.

3.1 Reaction pathways of eINT1

The ab initio calculations in Figs. 3 and 4 predicted that three different single-step processes exist for the energy-rich addition intermediate eINT1. First, the direct C–C bond cleavage of eINT1, through the transition state fTS1 with a barrier height of 16.2 kcal mol^{-1}, leads to formation of H_2CO (formaldehyde) + CH_3 in reaction (R1) ($\Delta H = -81.1$ kcal mol^{-1}). While the C–C bond in the process of breaking is elongated from 1.527 Å in eINT1 to 2.213 Å in fTS1, the C(1)–O bond is shortened from 1.365 to 1.227 Å (Fig. 4). Second, the direct rupture of the C(1)–H bond through the transition state aTS1, with a barrier height of 20.1 kcal mol^{-1}, leads to the formation of acetaldehyde (CH_3CHO) + H in reaction (R2) ($\Delta H = -77.3$ kcal mol^{-1}). Finally, the direct C(2)–H bond decomposition through the three-membered-ring transition state oTS1 results in the formation of c–CH_2OCH_2 (oxirane) + H in reaction (b3) ($\Delta H = -50.7$ kcal mol^{-1}). The corresponding barrier height was estimated to be 52.2 kcal mol^{-1}, which is significantly higher than that for the other two transition states, due to the high angle strain occurring in the formation of the cyclic three-membered transition state. Here, the barrier height appeared considerable, but were still well within the available energy of the eINT1 adduct. The optimized geometries of fTS1, aTS1, and oTS1 in Fig. 4 were found to be close to those of the corresponding products, indicating that the whole transition state shows the product-like features with late barriers.

After considering the barrier height and reaction exothermicity along the reaction coordinate, the major pathways were predicted to be reactions (R1) and (R2). In fact, two channels were found to be the most favorable in terms of both their thermodynamics and kinetics. The predicted major channels are also consistent with the gas-phase kinetic experiments, where two products, formaldehyde and acetaldehyde, were detected as the major species in the mass spectrometric analysis [7].

3.2 Reaction pathways of eINT2

The intermediate eINT2 showed a larger exothermicity of −102.3 kcal mol^{-1} compared to the other three intermediates (eINT1, eINT3, eINT4) as displayed in Fig. 3. Several reaction pathways starting from the highly energized eINT2 were predicted. First, O–H bond fission of eINT2 leads to the formation of acetaldehyde (CH_3CHO) + H in reaction (R2) by overcoming the aTS2 transition state. While the O–H bond in the process of breaking is elongated from 0.963 Å in eINT2 to 1.543 Å, the C–O bond is shortened from 1.375 to 1.233 Å (Fig. 4). Although the barrier height for bond rupture is 38.5 kcal mol^{-1}, it is still well within the available energy of the system, and the overall process was calculated to be highly exothermic by

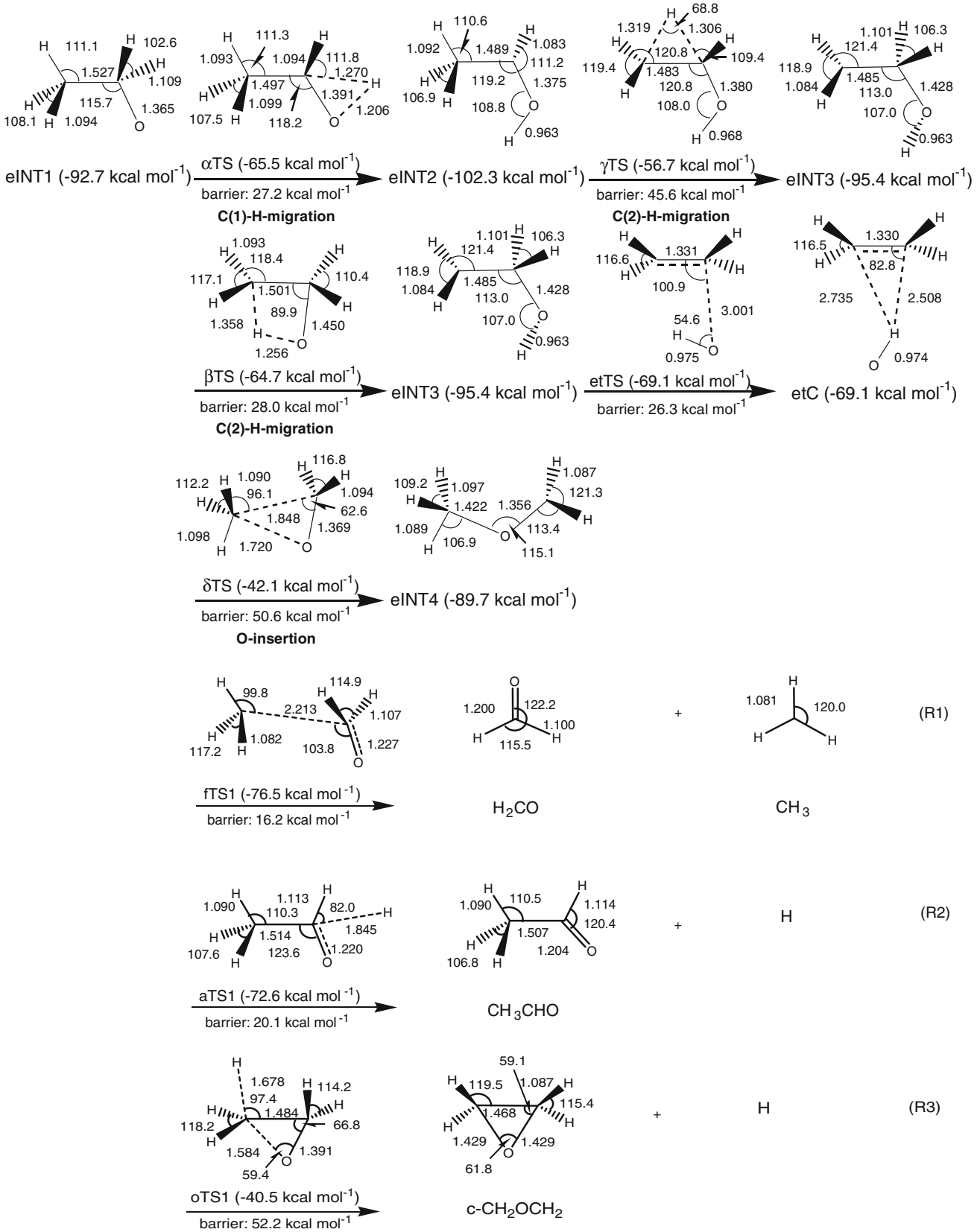

Fig. 4 Schematic pathways for various reactions from the reaction $O(^3P) + C_2H_5$ at 298.15 K at the CBS–QB3 level of theory. The values below the *arrows* denote the vibrationally adiabatic forward barrier heights

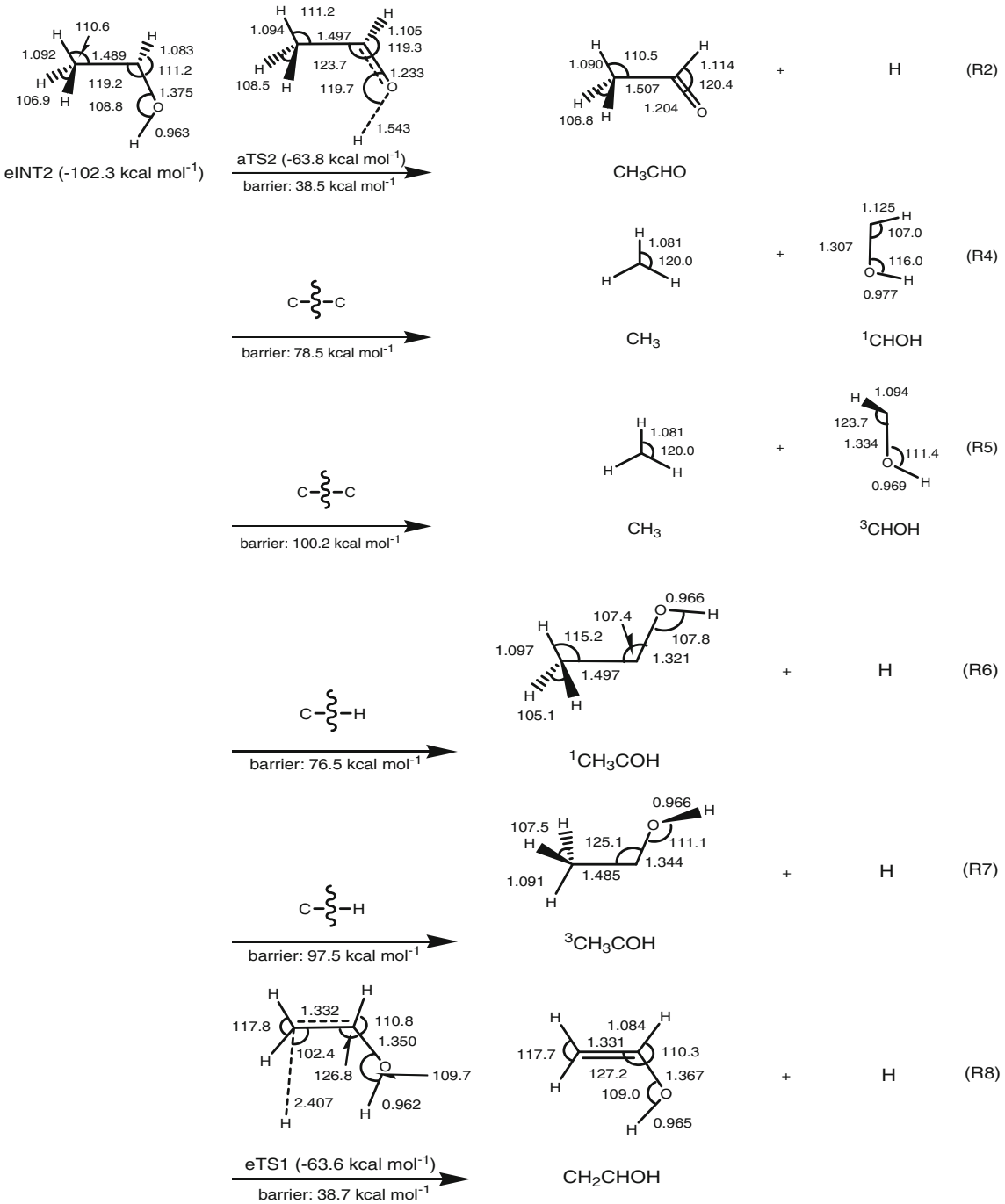

Fig. 4 continued

-77.3 kcal mol^{-1}. Second, four channels were calculated to be in competition for producing two pairs of carbene products. Direct C–C bond cleavage results in the formation of ^{1,3}CHOH + CH_3 in reactions (R4) and (R5) with respective energies of 78.5 and 100.2 kcal mol^{-1} needed for the reactions. In contrast, direct C(1)–H bond dissociation leads to the formation of $^{1,3}CH_3COH$ + H in reactions (R6) and (R7), with respective energies of 76.5 and 97.5 kcal mol^{-1} required for the reactions. The products ^{1}CHOH and $^1CH_3COH$ were calculated to be significantly more stable than their corresponding carbene isomers in the higher energy states, by 21.7 and 21.0 kcal mol^{-1}, respectively. Third, direct cleavage of the C(2)–H bond through transition state eTS1 with a barrier height of

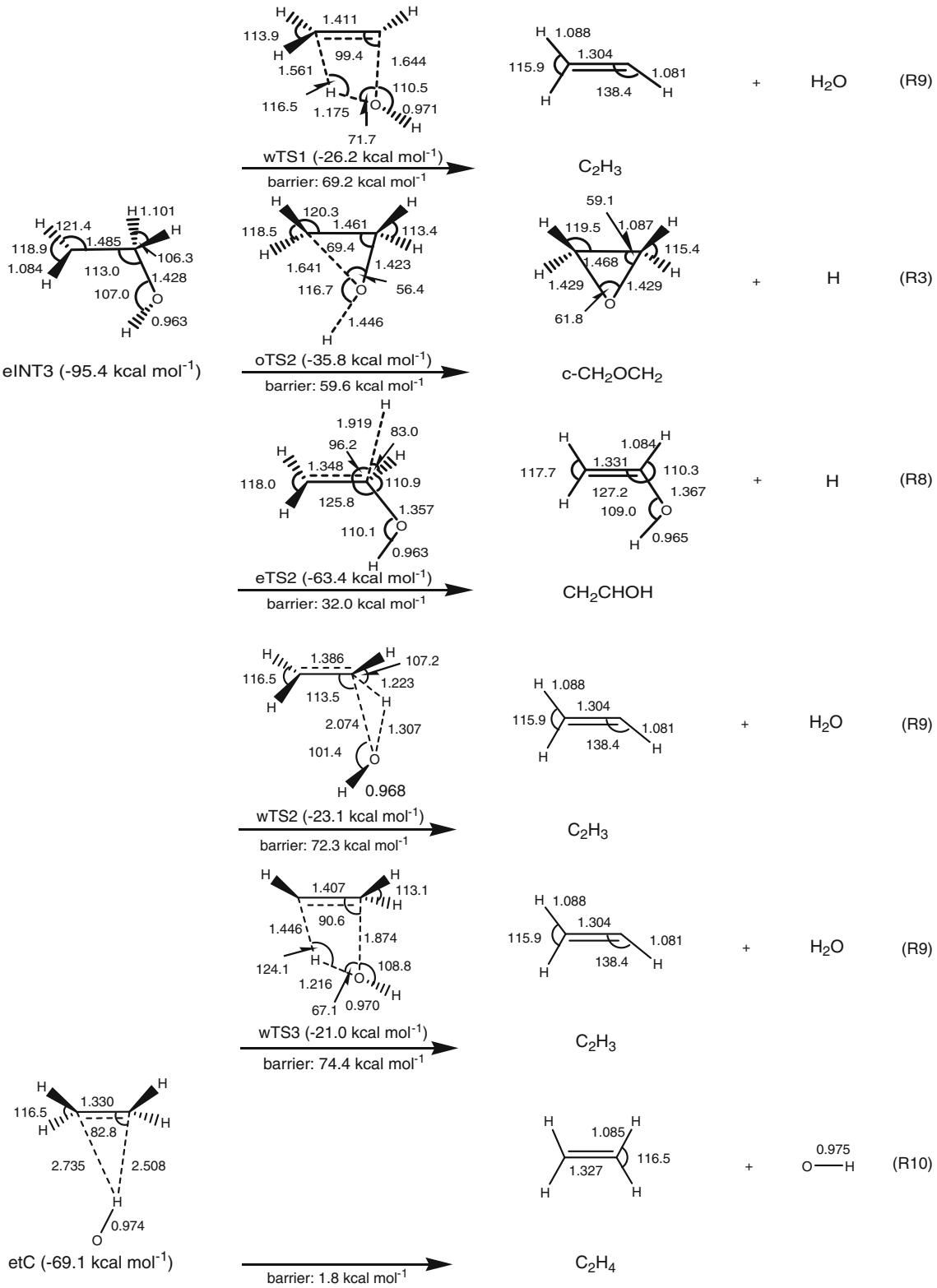

Fig. 4 continued

38.7 kcal mol^{-1} leads to the formation of CH_2CHOH (ethenol) + H in reaction (R8) ($\Delta H = -65.8$ kcal mol^{-1}). While the C(2)–H bond in the process of breaking is elongated from 1.092 Å in eINT2 to 2.407 Å, the C–C bond is shortened from 1.489 to 1.332 Å (Fig. 4). Finally, the H-atom shift from C(2) to O accompanied with the C(1)–O

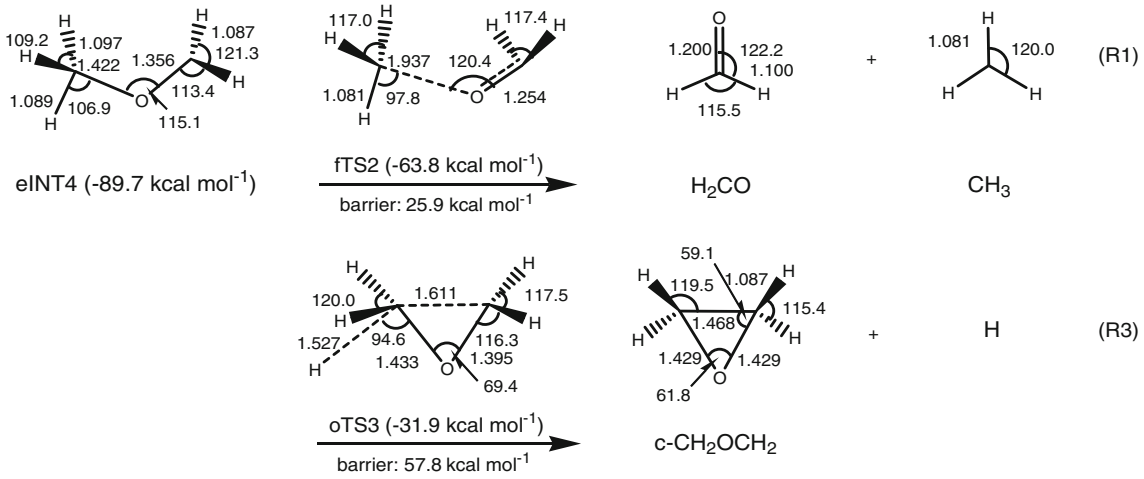

Fig. 4 continued

bond rupture through the transition state wTS1 results in the formation of $C_2H_3 + H_2O$ in reaction (R9) ($\Delta H = -75.8$ kcal mol^{-1}). The corresponding barrier height was estimated to be 69.2 kcal mol^{-1}, an unfavorably high value due to both the high angle strain occurring in the formation of the tight four-membered-ring transition state and the ensuing successive bond cleavage pathway.

3.3 Reaction pathways of eINT3

Five competing pathways were calculated for the energy-rich eINT3 in Fig. 4. First, the direct O–H bond rupture conversion through the three-membered-ring transition state oTS2 results in the formation of c–CH_2OCH_2 (oxirane) + H in reaction (R3) ($\Delta H = -50.7$ kcal mol^{-1}). The optimized geometry of oTS2 in Fig. 4 displays product-like features. The corresponding barrier height was estimated to be 59.6 kcal mol^{-1}, which is quite high due to the angle strain resulting from the formation of the oTS2 cyclic transition state. Second, direct cleavage of the C(1)–H bond through transition state eTS2 leads to formation of the CH_2CHOH (ethenol) + H in reaction (R8) ($\Delta H = -65.8$ kcal mol^{-1}), with a barrier height of 32.0 kcal mol^{-1}. While the C(1)–H bond, in the process of breaking, is elongated from 1.101 Å in eINT3 to 1.919 Å, the C–C bond is shortened from 1.485 to 1.348 Å. In contrast, the formation of $C_2H_3 + H_2O$ in reaction (R9) ($\Delta H = -75.8$ kcal mol^{-1}) results from two competing channels involving the H-atom migration to the neighboring oxygen atom. As can be seen in Fig. 4, both transition states wTS2 and wTS3 have the strained three- and four-membered-ring geometries; the corresponding respective barrier heights were estimated to be 72.3 and 74.4 kcal mol^{-1}, stemming from the high angle strain occurring in the formation of tight cyclic transition states. Finally, the pathway of eINT3, leading to the formation of C_2H_4 (ethene) + OH in reaction (R10) ($\Delta H = -67.3$ kcal mol^{-1}), involves a peculiar isomerization process as the initial step. After the direct C(1)–OH bond rupture through the etTS transition state, with a barrier height of 26.3 kcal mol^{-1}, the H-atom of the OH radical is rotated toward C_2H_4 to form an apparent van der Waals complex etC. The complex has a weakly bound structure, in which the electron-deficient H-atom of the OH radical perpendicularly interacts with the C=C π bond of C_2H_4. The OH–C bond length and the stabilization energy with respect to products $C_2H_4 + OH$ were estimated to be 2.508 Å and -1.8 kcal mol^{-1} at the CBS-QB3 level of theory, respectively. Here, it should be noted that due to the very shallow character of the etTS-etC part of the pathway on the potential energy surface, the energy difference between the etTS and etT structures could be dependent on the computational methods. The results were quite consistent with the recent theoretical studies on the reverse reaction of ethylene + OH, in which as the OH radical attacks ethylene, the association complex was predicted to exist as the pre-reaction association adduct along the entrance channel [43–46].

3.4 Reaction pathways of eINT4

The calculations predicted two different reaction pathways for eINT4. The direct C(2)–O bond cleavage of eINT4, through the transition state fTS2, leads to formation of formaldehyde (H_2CO) + CH_3 in reaction (R1). While the C(2)–O bond in the process of breaking is elongated from 1.422 Å in eINT4 to 1.937 Å in fTS2, the C(1)–O bond is shortened from 1.356 to 1.254 Å (Fig. 4). The barrier height for the bond fission is 25.9 kcal mol^{-1}, and the overall process was calculated to be highly exothermic by

−81.1 kcal mol^{-1}. In contrast, the direct C(2)–H bond decomposition through the three-membered-ring transition state oTS3 results in the formation of c–CH_2OCH_2 (oxirane) + H in reaction (R3) ($\Delta H = -50.7$ kcal mol^{-1}). The formation of the cyclic transition state entails overcoming a high barrier height of 57.8 kcal mol^{-1}. Both channels also show high reaction exothermicities due to the formation of both stable closed-shell molecules and radical species. The optimized geometry of oTS3 in Fig. 4 shows the features of a product-like late barrier. The eINT4-oTS3 pathway was found to be in competition with the eINT1-oTS1 and eINT3-oTS2 pathways described in previous sections.

3.5 A direct, barrierless abstraction pathway for $O(^3P) + C_2H_5 \rightarrow CH_2CH_2 + OH$

In comparison with the aforementioned eINT3-etTS-etC. addition pathway, which has not been reported in the previous kinetic experiments, a second, straightforward and facile pathway in reaction (R10) was predicted to proceed through the direct H-atom abstraction shown in Figs. 3 and 5. The abstraction mechanism has been commonly observed in the reactions of $O(^3P)$ with closed-shell hydrocarbon molecules [21–24]. The abstraction reaction results from the dynamics of a direct H-atom transfer via a collinear transition state. In general, for a series of primary, secondary, and tertiary hydrocarbon molecules, as the reaction exothermicity increased, the barrier to the abstraction of the H-atom from the C–H bond of a hydrocarbon molecule gradually decreased from ~7 to ~3 kcal mol^{-1}, as summarized in Fig. 5.

For reaction (R10), the entrance barrier along the reaction coordinate was calculated to be negligible, like that in the barrierless addition processes. The absence of a barrier height can also be attributed to the unusually small C–H bond dissociation energy of C_2H_5 (BDE = 36.2 kcal mol^{-1}) and the high reaction exothermicity of $\Delta H = -67.3$ kcal mol^{-1}, leading to formation of a stable ethylene product. Similar barrierless systems can be found in the reactions of allyl and *t*-butyl radicals, as indicated in Fig. 5. Both radical systems show the unusually small C–H bond dissociation energy (BDE = 57.6 and 35.5 kcal mol^{-1} for allyl and *t*-butyl, respectively) and the high reaction exothermicities ($\Delta H = -46.0$ and -67.2 kcal mol^{-1} for allyl and *t*-butyl, respectively) [31–33]. This observation can also be rationalized in terms of the Hammond postulate, which states that for exothermic reactions, low-activation barriers indicate the structural similarity of the reactants and transition states as that in the title reaction [47]. For the reaction channel (R10), the extent is particularly significant due to the high exothermicity and the very early barrier in the entrance channel, giving rise to a direct, barrierless abstraction channel [48].

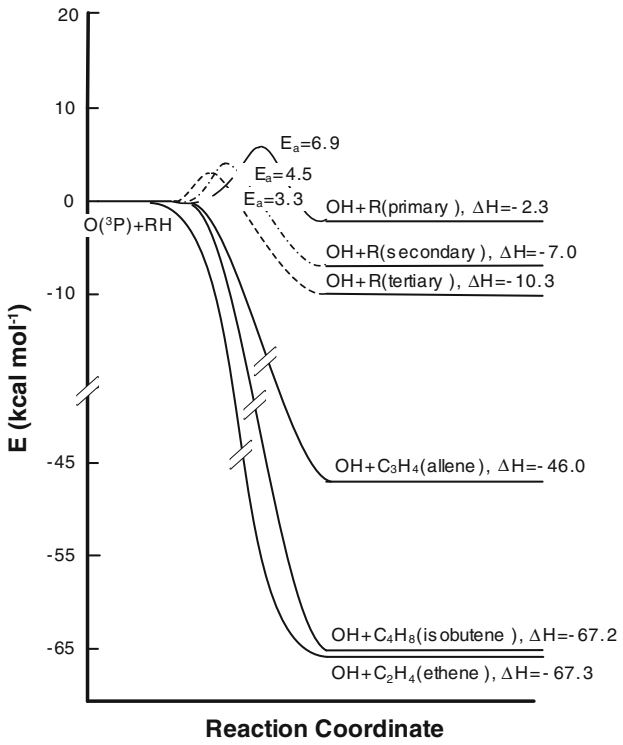

Fig. 5 Comparative schematic energy diagram for the H-atom abstraction processes in the reactions of $O(^3P)$ with C_2H_5 and a series of hydrocarbon molecules and radicals

3.6 Comparison with the crossed-beam experiments: statistical versus dynamic

It is worth comparing the presented theoretical predictions to the recent experimental results for channel (R10). The nascent rovibrational state distributions of the OH product investigated by high-resolution, laser-induced fluorescence (LIF) spectroscopy in a crossed-beam configuration revealed bimodal rotational excitations consisting of low- and high-N'' components with the ratio of about 1.5:1. In particular, the high rotational temperatures for high-N'' components were estimated to be up to 4,750 K (Fig. 6a). Neither spin–orbit nor Λ-doublet propensities in the ground and first excited vibrational states were observed. The averaged vibrational population ($P_{v''}$), partitioning with respect to the low-N'' components of the $v'' = 0$ level, showed population inversion with a ratio of $P_0 : P_1 = 1 : 1.06$, which is consistent with the observed nonstatistical inversion using time-resolved FT-IR spectroscopy [4, 5, 19].

To better characterize such nascent populations, the statistical surprisal approach based upon the calculation of the prior distribution was used. The prior approach assumes

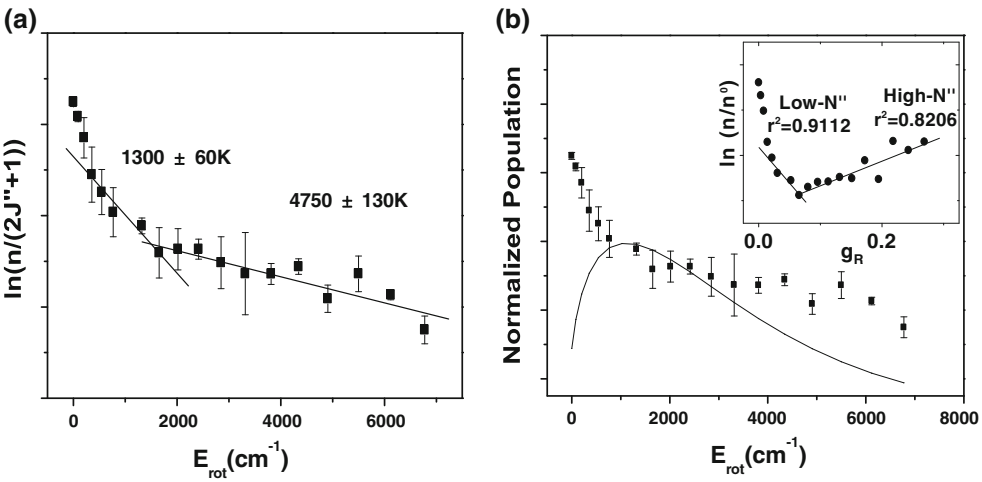

Fig. 6 The nascent OH (the F_1 spin–orbit state) produced in the reaction of $O(^3P) + C_2H_5$: **a** Boltzmann plot of the nascent OH distribution as a function of rotational energy; **b** normalized rotational populations (*filled circles*) with a statistical prior (−) plot. The *inset* represents a rotational surprisal plot as a function of the rotational fraction of the available energy g_R

that for the decomposing energized intermediate, all allowed quantum states of products are equally accessible and that the product state distribution is solely determined by the available volumes in phase space of the two fragment products. The prior distribution shown in Fig. 6b appeared nearly Boltzmann-type over the whole range. The comparison of the prior plot with the LIF spectrum of nascent OH distributions demonstrates significant rotational excitations, together with an evident bimodal feature in $\upsilon'' = 0$. The statistical surprisal analysis was applied to deduce the relative contribution of each component in the bimodal distribution of the $\upsilon'' = 0$ level. The surprisal represents the extent of the deviation from the statistical distribution; the rotational surprisal (I) is given by:

$$I(f_r/f_v) = -\ln[n(\upsilon'', J'')/n^o(\upsilon'', J'')],$$

where f_r and f_v are the respective fractions of the rotational and vibrational energies of the OH products [49]. The terms $n(\upsilon'', J'')$ and $n^o(\upsilon'', J'')$ are the experimental and prior populations in a specific rovibrational state, respectively. As shown in the inset of Fig. 6b, however, it was not possible to deconvolute the rotational populations due to the poor surprisal fit. This discrepancy between the nascent distributions and the prior estimations strongly means that the statistical picture of the prior theory is not entirely appropriate to depict the population distributions of the OH products, and that the observed experimental distributions evidently exhibit dynamic characteristics in the formation of ethene + OH.

The observed distinctive bimodal distributions and vibrational population inversion in reaction channel (R10) can be properly explained by the competing abstraction and addition mechanisms described in the previous sections. The major pathway can be ascribed to the direct abstraction process leading to the inversion of the vibrational populations, while the minor pathway is described in terms of the short-lived, addition complexes responsible for the hot rotational distributions obtained in the $\upsilon'' = 0$ level. Especially, unusually high rotational temperatures for high-N'' components can be understood in terms of a peculiar decomposition process through the eINT3-etTS-etC-(R10) pathway. At the moment of the direct C(1)–OH bond rupture through the etTS transition state, a strong torque is expected to be exerted on the OH radical bent with respect to the ethylene moiety, which results in an usually high rotational excitation. The observed nonpreferential dynamic propensities for the Λ-doublet and spin–orbit distributions in all of the examined vibrational states can be understood in terms of the fast and random decomposition of the short-lived, dynamic intermediates along the reaction coordinate, although a detailed adiabatic correlation diagram, including all possible orientations of the $O(^3P)$ approach and spin–orbit levels, is not available.

4 Conclusions

Ab initio calculations based upon the density functional method and complete basis set model were carried out in order to study the radical–radical reaction of $O(^3P) + C_2H_5$. Two distinctive pathways were calculated to be in competition: addition and abstraction. The barrierless addition of $O(^3P)$ to C_2H_5 resulted in the formation of energy-rich intermediates that led to various products through direct elimination or isomerization–elimination processes. The major pathways were predicted to be the formation of $H_2CO + CH_3$ and $CH_3CHO + H$ through the low-barrier, single-step cleavages of the addition intermediates. Unlike previous kinetic results, proposed to proceed only through the direct H-atom abstraction process, the direct, barrierless H-atom abstraction mechanism producing $CH_2CH_2 + OH$ was calculated to compete with the addition processes. The OH reaction channels were compared with the crossed-beam investigations to understand

the kinetic and dynamic characteristics, respectively. The work herein represents a step forward in understanding the elementary oxidation reactions of saturated hydrocarbon radicals. Extensive ab initio calculations, combined with crossed-beam experiments on several radical–radical reactions of second-row atomic species with organic hydrocarbon radicals, are currently being conducted. It is the hope of the authors that the gas-phase reaction dynamics studies presented will provide valuable mechanistic insights into radical–radical reactions at the molecular level that have, thus far, remained unexplored.

Acknowledgments This work was supported by National Research Foundation of Korea Grant funded by the Korean Government (2010-0014418) and Priority Research Centers Program through the National Research Foundation of Korea (NRF) funded by the Ministry of Education, Science and Technology (NRF20100020209).

References

1. Choi JH (2006) Int Rev Phys Chem 25:613 (references therein)
2. Donalson DJ, Okuda IV, Sloan J (1995) J Chem Phys 193:37
3. Min Z, Quandt RW, Wong TH, Bersohn R (1999) J Chem Phys 111:7369
4. Lindner J, Loomis RA, Klaassen JJ, Leone SR (1998) J Chem Phys 108:1944
5. Reid JP, Marcy TP, Kuehn S, Leone SP (2000) J Chem Phys 113:4572
6. Slagle IR, Sarzynski D, Gutman D, Miller JA, Melius CF (1988) J Chem Soc Faraday Trans II 84:491
7. Hoyermann K, Olzmann M, Seeba J, Viskolcz B (1999) J Phys Chem A 103:5692
8. Hack W, Hoyermann K, Olzmann M, Zeuch T (2002) Proc Combust Inst 29:1247
9. Kwon HC, Park JH, Lee H, Kim HK, Choi YS, Choi JH (2002) J Chem Phys 116:2675
10. Park JH, Lee H, Kwon HC, Kim HK, Choi YS, Choi JH (2002) J Chem Phys 117:2017
11. Lee H, Joo SK, Kwon LK, Choi JH (2003) J Chem Phys 119:9337
12. Lee H, Joo SK, Kwon LK, Choi JH (2004) J Chem Phys 120:2215
13. Joo SK, Kwon LK, Lee H, Choi JH (2004) J Chem Phys 120:7976
14. Nam MJ, Youn SE, Li L, Choi JH (2005) J Chem Phys 123:211105
15. Nam MJ, Youn SE, Choi JH (2006) J Chem Phys 124:104307
16. Kwon LK, Nam MJ, Youn SE, Joo SK, Lee H, Choi JH (2006) J Chem Phys 124:204320
17. Youn SE, Ok YH, Choi JH (2008) Chem phys chem 9:1099
18. Park YP, Kang KW, Jung SH, Choi JH (2010) J Phys Chem A 114:4891
19. Park YP, Kang KW, Jung SH, Choi JH (2010) Phys Chem Chem Phys 12:7098
20. Kohn DW, Clauberg H, Chen P (1992) Rev Sci Instrum 63:4003
21. Sweeney GM, McKendrick KG (1997) J Chem Phys 106:9182
22. Sweeney GM, Watson A, McKendrick KG (1997) J Chem Phys 106:9172
23. Kleimermanns K, Luntz AC (1982) J Chem Phys 77:3533
24. Andresen P, Luntz AC (1980) J Chem Phys 72:5842
25. Knyazev VD (2001) J Phys Chem A 106:8741
26. Marcy TP, Diaz RR, Heard D, Leone SR, Harding LB, Klippenstein SJ (2001) J Phys Chem A 105:8361
27. Yagi K, Takayanagi T, Taketsugu T, Hirao K (2004) J Chem Phys 120:10395
28. Harding LB, Klippenstein SJ, Georgievskii Y (2005) Proc Combust Inst 30:985
29. Gupta A, Singh RP, Singh VB, Mishra BK, Sathyamuryhy N (2007) J Chem Sci 119:457
30. Yong Y, Weijun Z, Xiaoming G, Shixin P, Jie S, Wei H, Jun Q (2005) Chin J Chem Phys 18:515
31. Nam MJ, Youn SE, Choi JH (2006) ChemPhysChem 7:2526
32. Park JH, Lee H, Choi JH (2003) J Chem Phys 119:8966
33. Lee H, Nam MJ, Choi JH (2006) J Chem Phys 124:044311
34. Baulch DL, Bowman CT, Cobos CJ, Cox RA, Just Th, Kerr JA, Pilling MJ, Stocker D, Troe J, Tsang W, Walker RW, Warnatz J (2005) J Phys Chem Ref Data 34:757
35. Petersson GA, Al-Laham MA (1991) J Chem Phys 94:6081
36. Petersson GA, Tensfeldt TG, Montgomery JA Jr (1991) J Chem Phys 94:6091
37. Montgomery JA Jr, Ochtersk JW, Petersson GA (1994) J Chem Phys 101:5900
38. Baker J, Muir M, Andzelm J (1995) J Chem Phys 102:2063
39. Ochterski JW, Petersson GA, Montgomery JA Jr (1996) J Chem Phys 104:2598
40. Montgomery JA Jr, Frisch MJ, Ochterski JW, Petersson GA (1999) J Chem Phys 110:2822
41. Lee C, Yang W, Parr RG (1988) Phys Rev B 37:785
42. Frisch MJ, Trucks GW, Schlegel HB, Scuseria GE, Robb MA, Cheeseman JR, Zakrzewski VG, Montgomery JA Jr, Stratmann RE, Burant JC, Dapprich S, Millam JM, Daniels AD, Kudin KN, Strain MC, Farkas O, Tomasi J, Barone V, Cossi M, Cammi R, Mennucci B, Pomelli C, Adamo C, Clifford S, Ochterski J, Petersson GA, Ayala PY, Cui Q, Morokuma K, Malick DK, Rabuck AD, Raghavachari K, Foresman JB, Cioslowski J, Ortiz JV, Baboul AG, Stefanov BB, Liu G, Liashenko A, Piskorz P, Komaromi I, Gomperts R, Martin RL, Fox DJ, Keith T, Al-Laham MA, Peng CY, Nanayakkara A, Gonzalez C, Challacombe M, Gill PMW, Johnson B, Chen W, Wong MW, Andres JL, Gonzalez C, Head-Gordon M, Replogle ES, Pople JA (2003) Gaussian 03, revision B 01. Gaussian, Inc., Pittsburgh
43. Zhu RS, Park J, Lin MC (2005) Chem Phys Lett 408:25
44. Senosiain JP, Klippenstein SJ, Miller JA (2006) J Phys Chem A 110:6960
45. Xu ZF, Xu K, Lin MC (2009) ChemPhysChem 10:972
46. Liu GX, Ding YH, Li ZS, Fu Q, Huang XR, Sun CC, Tang AC (2002) Phys Chem Chem Phys 4:1021
47. Hammond GS (1955) J Am Chem Soc 77:334
48. Steinfeld JI, Francisco JS, Hase WL (1999) Chemical kinetics and dynamics. Prentice Hall, New Jersey
49. Baer T, Hase WL (1996) Unimolecular reaction dynamics. Oxford University, New York